Reports

A Combined Irradiance-Transmittance Solar Spectrum and Its Application to Photovoltaic Efficiency Calculations

Abstract. *SOLTRAN is a flexible computer model for the direct solar beam intensity spectrum at the earth's surface. It has been derived by combining the extraterrestrial solar spectrum with the atmospheric transmittance spectrum. Application of SOLTRAN to the calculation of the potential efficiency of photovoltaic cells demonstrates the effect of atmospheric absorption bands. These bands prevent unequivocal assignment of optimum energy gap values.*

We report the development of a new solar power density spectrum, SOLTRAN, and its application to the calculation of maximum potential efficiencies of photovoltaic cells. Earlier solar spectra in the wavelength (λ) region between 0.8 and 1.0 μm are discussed in some detail because of their interest in relation to photovoltaic converters. It is shown that SOLTRAN correctly incorporates the accepted water absorption bands, as do Moon's spectra (*1*). The terrestrial spectra reported by Gates (*2*) and by Thomas and Thekaekara (*3*) are found to be incorrect in this wavelength regime.

SOLTRAN is a combined solar irradiance–atmospheric transmittance computer model, capable of predicting the direct (that is, excluding circumsolar radiation) solar beam intensity spectrum (0.25 to 3.0 μm) at the earth's surface (*4*). At present, the spectral resolution is 200 cm^{-1}. The extraterrestrial solar spectrum (*3*) was folded into a modified atmospheric transmittance program, LOWTRAN (*5*), and the solar vector geometry. SOLTRAN produces spectra as a function of the following parameters.

1) Six atmospheric conditions: 1962 U.S. standard; tropical, 15°N; midlatitude summer, 45°N, July; midlatitude winter, 45°N, January; subarctic summer, 60°N, July; and subarctic winter, 60°N, January. Actual temperature, pressure, and water vapor data can be put in at altitude increments of 1 km.

2) Relative air mass for solar elevations of 0° to 90°, including the influence of atmospheric refraction.

3) Site altitude.

4) Aerosols: a surface visual range is utilized to define atmospheric clarity (a measure of aerosol concentration) and its altitude profile. Actual aerosol data can be incorporated.

Figure 1 shows the spectrum employed in this report for Golden, Colorado, with the following parameters: midlatitude summer, 45°N, July; relative air masses 0, 1, and 2; site altitude, 1707 m; and a clear atmosphere, visibility 35 km. Under these conditions, the air mass 1 (AM1) power density is 101 mW/cm^2. Comparison of SOLTRAN spectra with earlier data has revealed an interesting discrepancy between the SOLTRAN AM1 spectrum and the AM1 spectrum calculated by Thomas and Thekaekara (TT) (*3*), which is based on the earlier data of Gates (*2*) and nearly identical to his spectrum. Gates's work and technique have been used by numerous other investigators to produce similar solar power density spectra. Visual comparison of the AM1 spectrum of Fig. 1 and that of (*2, 3*) reveals a discrepancy in the region λ = 0.8 to 1.0 μm. The earlier spectra of (*2, 3*) show strong attenuation between 0.84 and 0.95 μm, whereas the SOLTRAN spectrum shows little attenuation except for the narrow band at 0.94 μm.

This discrepancy may indicate an error in spectral measurement or evaluation procedures that should be corrected. Also, the width and intensity of the band is of interest with regard to photovoltaic conversion, as it is used to argue in favor of GaAs (long-wavelength cutoff λ_{gap} = 0.868 μm) over InP (λ_{gap} = 0.926 μm). Therefore we carried out a preliminary investigation by directly comparing the fractional atmospheric transmittance of SOLTRAN to the TT data.

The major source of atmospheric attenuation in the region λ = 0.8 to 1.0 μm is water vapor. The available TT data are for sea level with a precipitable water content of 20 mm. The SOLTRAN program for sea level at midlatitude includes 34 mm of precipitable water. A 34-mm precipitable water content in the TT data would cause even deeper water-related

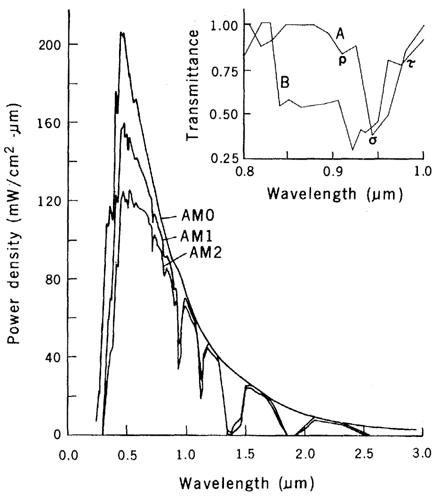

Fig. 1. Typical SOLTRAN spectra for air mass 0, 1, and 2 (*AM0, AM1*, and *AM2*) at midlatitude (Golden, Colorado) with a visibility of 35 km. The inset shows (*A*) the calculated water vapor transmittance curve for SOLTRAN at sea level and (*B*) Thomas and Thekaekara's (*3*) data showing the water vapor bands ρ, σ, and τ.

absorption than shown in (*2, 3*). The spectral shape however, which is the more important question to be addressed, will remain the same. In the inset of Fig. 1, relative transmittances are plotted for SOLTRAN (curve *A*) and for TT (curve *B*). As expected, a major discrepancy exists. SOLTRAN exhibits the well-known ρ and σ water absorption bands (*6*), but it does not show the τ band because the resolution is currently insufficient. Curve *B* is anomalous; it is not attributable to water vapor. A comparison with the data of Moon (*1*) shows that the structure of Moon's spectral attenuation curves at $\lambda = 0.8$ to 1.0 μm is similar to that of SOLTRAN. Further analysis is required to explore the anomalous attenuation reported by Thomas and Thekaekara and by Gates.

Solar cell short-circuit currents have been derived from the SOLTRAN model and incorporated in efficiency calculations for multijunction cells. The economic prospects of multijunction converters to be used in concentrator systems have stimulated calculations for cascaded cells with individual narrow spectral responses (*7, 8*). In the analysis reported here a simple phenomenological diode model (*9*) was employed together with a constant fill factor. (Note that the fill factor may vary with changes in the absorbing band gap and with solar intensity.) Series optical and electrical structures were assumed. These photovoltaic efficiency calculations show that the water absorption bands prevent the unequivocal identification of maxima in the efficiency versus energy gap functions.

The cell efficiency η was computed from the common short-circuit current density J_{sc}, the sum of the open-circuit voltages V_{oc} for the individual layers, a common curve fill factor $F = 0.80$, and the incident solar power flux density P as

$$\eta = \frac{J_{sc} V_{oc} F}{P} \qquad (1)$$

The short-circuit current density J_{sc} was calculated by assuming a quantum efficiency Q of 0.90, uniform over the spectrum to which a specific diode can be sensitive according to band gap consideration. Band gaps were adjusted to provide identical photocurrents in each diode.

$$J_{sc} = \frac{qQ}{N} \int_{\lambda_0}^{\lambda_{gap}} \phi(\lambda) d\lambda \qquad (2)$$

where q is the electronic charge, $\phi(\lambda)$ the photon flux density derived from SOLTRAN, λ_0 the short- and λ_{gap} the long-wavelength cutoff, respectively, and N the number of active layers. Expressed in terms of the absorber material with the lowest energy gap, $\lambda_{gap} = hc/E_g$, with h being Planck's constant and c the velocity of light.

The open-circuit voltage V_{oc} was calculated for devices whose dark current-voltage characteristics are controlled by bulk injection. This procedure does not take into account the transition from bulk-controlled to space charge-controlled current when passing from members of a multijunction device with large band gaps to ones with small band gaps, nor does it consider nonideal contributions, as from bulk or series resistance. However, the results clearly delineate the regime of attainable efficiencies and of optimum band gap values.

The open-circuit voltage is represented by

$$V_{oc} = \sum_{i=1}^{N} \frac{AkT}{q} \ln \left(\frac{J_{sc}}{J_{0i}} + 1 \right) \qquad (3)$$

where A is the diode factor, equal to 1 for diffusion-controlled current and to 2 for recombination-controlled current, k the Boltzmann constant, and T the absolute temperature. The reverse saturation current density, J_0, was expressed as a function of the energy gap E_g:

$$J_0 = B_0 \exp \left(\frac{E_g}{BkT} \right) \qquad (4)$$

The constant B_0 was set to a value of 15, in combination with A = B (either 1 or 2), to provide realistic values of J_0. No spurious optical losses (arising from reflection, lower than band gap absorption, and so on) were taken into account.

The maximum efficiencies (η_{max}) for

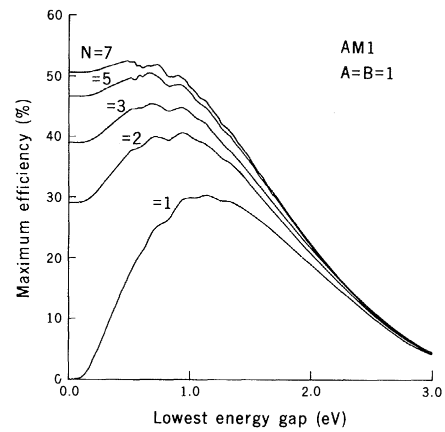

Fig. 2. Multilayer cell efficiency for one to seven absorber layers.

cells with up to seven active layers are shown in Fig. 2 as a function of the value of the lowest energy gap. Large numbers of active layers appear unrealistic with present semiconductor technology. However, the calculations also provide a useful estimate of efficiencies attainable through other technologies with the potential for photovoltaic conversion. An example could be a multilayer device produced from a series of organic semiconducting dyes, each with its characteristic narrow spectral response. Again, it is evident that the atmospheric absorption bands are positioned such as to level out what would otherwise be flat but well-defined efficiency maxima. Figure 2 also demonstrates the diminishing incremental efficiency per added layer. In fact, it is evident that optical losses somewhat larger than those implied by the assumed quantum efficiency of 0.90 could lead to a maximum in the curve of η_{max} versus N, an effect that has been recognized in studies of spectral splitting (*8*).

PHILIP J. IRELAND
SIGURD WAGNER
LAWRENCE L. KAZMERSKI
Photovoltaics Branch,
Solar Energy Research Institute,
Golden, Colorado 80401
ROLAND L. HULSTROM
Energy Resource Assessment Branch,
Solar Energy Research Institute

References and Notes

1. P. Moon, *J. Franklin Inst.* **20**, 600 (1940).
2. D. M. Gates, *Science* **151**, 523 (1966).
3. A. P. Thomas and M. P. Thekaekara, in *Sharing the Sun—Solar Technology in the Seventies, Winnipeg, Canada* (American Section of the International Solar Energy Society, Fla., 1976), vol. 1, p. 338.
4. Detailed information about SOLTRAN may be obtained from R.L.H.
5. J. E. A. Selby and R. A. McClatchey, *Air Force Geophys. Lab. Tech. Rep. AFGL-TR-75-0255, ERP 513, AD-AO17734* (1975). The Air Force Geophysics Laboratory has expended significant effort in developing LOWTRAN. The Solar Energy Research Institute has applied LOWTRAN to calculate the solar spectrum terrestrial transmittance.

6. R. M. Goody, *Atmospheric Radiation*, vol. 1, *Theoretical Basis* (Clarendon, Oxford, 1964).
7. N. S. Alvi, C. E. Backus, G. W. Masden, in *Proceedings of 12th Photovoltaic Specialists Conference* (IEEE, New York, 1976), p. 948; J. J. Loferski, in *ibid.*, p. 957.
8. G. W. Masden and C. E. Backus, in *Proceedings of 13th Photovoltaic Specialists Conference* (IEEE, New York, 1978), p. 853; R. L. Moon, L. W. James, H. A. Vanderplas, Y. G. Chai, G. A. Antypas, in *ibid.*, p. 859; A. Bennett and L. C. Olsen, in *ibid.*, p. 868; M. F. Lamorte and D. Abbott, in *ibid.*, p. 874; J. A. Cape, J. S. Harris, R. Sahai, in *ibid.*, p. 881; L. M. Fraas and R. C. Knechtli, in *ibid.*, p. 886; A. G. Milnes, in *ibid.*, p. 892; M. Arienzo and J. J. Loferski, in *ibid.*, p. 898.
9. J. J. Loferski, *J. Appl. Phys.* **27**, 777 (1956).

4 December 1978; revised 1 March 1979

Galápagos Hydrothermal Mounds: Stratigraphy and Chemistry Revealed by Deep-Sea Drilling

Abstract. *The Galápagos mounds sea-floor hydrothermal system is at least 300,000 years old and once produced manganese-poor sediments, which nearly blanketed the area of the present mounds field. Present-day mound deposits are limited manganese-rich exposures, suggesting that the system has changed from rock- to water-dominated and has diminished in intensity with time.*

In May 1977 the drilling ship *Glomar Challenger*, during Deep Sea Drilling Project (DSDP) leg 54, found and cored small mounds of sea-floor hydrothermally produced sediments in an area of high heat flow 22 km south of the Galápagos Rift (*1, 2*). A deep tow survey had shown the mounds to be arrayed in rows, strips, and ridges above small, near-vertical basement faults, and to be up to 10 m high and 25 m in diameter (*3*). They also have high water temperatures; have surfaces consisting of dark Fe-Mn oxides, brown to yellow iron oxyhydroxides, and clay minerals; and support thriving communities of macrobenthos (*4*).

The drilling provided the first complete sediment sections through any sea-floor hydrothermal deposits and reached basaltic basement in four places, penetrating as much as 45 m below the sediments in one hole. We have already presented data (*5*) on the composition of the sediments and basalts cored in the four holes at DSDP site 424, showing the sediments to be similar to reported hydrothermal deposits from the Mid-Atlantic Ridge (*6*) and the Gulf of Aden (*7*). Here, we explore the consequences of the stratigraphy and transition metal chemistry of the deposits.

The four holes were drilled along a north-south line and spaced about 300 m apart (Fig. 1). Holes 424 and 424A were directly on mounds, and hole 424B was in a flat area between them. Hole 424C was not completely cored beacuse of time constraints, but provided an undisturbed "mud-line" core (the top 10 cm are oxidized surface sediments), allowing us to reconstruct the sediment profile (Fig. 1) from the deep tow survey (*3*) by using water depths determined by drill-string length (rather than acoustically). This confirmed that we had cored two elevated mound structures in holes 424 and 424A.

Three types of sediments were recovered: (i) dark gray, semilithified, soft but brittle Fe-Mn oxides and clays; (ii) a distinct green mud, consisting almost entirely of Fe-rich, Mn-poor smectites (*5*); and (iii) foraminifer-nannofossil ooze with a moderate siliceous component (Fig. 1). This represents the stratigraphic sequence in the two holes on mounds. The process of drilling severely mixed the dark gray and green sediments at the top of the two holes, but individual chips of the dark gray material consist of two mineralogic end-members, Fe-Mn oxides (mainly todorokite with some birnessite) and Fe-rich, Mn-poor clay minerals identical to the more uniform green muds deeper in the holes. Green muds form discrete thin beds in holes 424 and 424A and a bed several meters thick in hole 424B, sandwiched between two layers of foraminifer-nannofossil ooze (Fig. 1); these contain no manganese oxides. About 12 to 15 m of foraminifer-nannofossil ooze occurs at the base of holes 424, 424A, and 424B.

Hole 424B is important because it represents the regional sediment blanket, which is uniformly about 25 to 30 m thick in the area. Two reflectors in this sediment blanket, thought to be ash layers, were found by the deep tow survey (*3*). However, hole 424B has no ash layers. Instead, the top and bottom of the green mud layer in that hole provide sufficient acoustic impedance contrasts (the muds are about 30 percent denser than the calcareous oozes) to explain the reflectors. Consequently, we believe that the green muds at hole 424B represent a nearly continuous layer between older and younger calcareous oozes throughout the area of the mounds field [about 350 km^2 (*1, 3*)]. The age of basement at site 424 estimated from sea-floor magnetics (*1*) and shipboard biostratigraphy is about 600,000 years. Assuming a uniform carbonate sedimentation rate (*8*) and an effectively "instantaneous" rate for the nearly carbonate-free green muds, the deepest green muds in hole 424B (15 m above basement) were first deposited about 300,000 years ago. The basal reflector pinches out about 12 km from the Galápagos Rift on crust about 300,000 years old [assuming uniform sea-

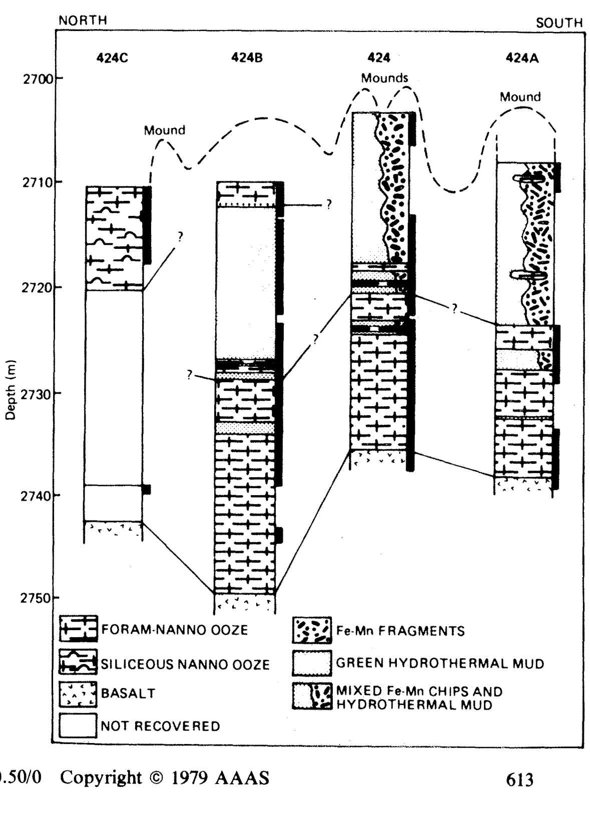

Fig. 1. Lithologic columns for holes 424, 424A, and 424C (sediments and top of basement only). Columns to the right of each lithologic column show recovery for each core, with the recovered interval beginning at the top of each core (DSDP convention). Lithologic boundaries have been placed by assuming that the core recovery is representative of the entire 9.5-m interval of each core.

0036-8075/79/0511-0613$00.50/0